

Digital Twin-Driven All-Solid-State Battery: Unraveling the Physical and Electrochemical Behaviors

Joonam Park, Kyu Tae Kim, Dae Yang Oh, Dahee Jin, Dohwan Kim, Yoon Seok Jung,* and Yong Min Lee*

The digital twin technique has been broadly utilized to efficiently and effectively predict the performance and problems associated with real objects via a virtual replica. However, the digitalization of twin electrochemical systems has not been achieved thus far, owing to the large amount of required calculations of numerous and complex differential equations in multiple dimensions. Nevertheless, with the help of continuous progress in hardware and software technologies, the fabrication of a digital twin-driven electrochemical system and its effective utilization have become a possibility. Herein, a digital twin-driven all-solid-state battery with a solid sulfide electrolyte is built based on a voxel-based microstructure. Its validity is verified using experimental data, such as effective electronic/ionic conductivities and electrochemical performance, for $\text{LiNi}_{0.70}\text{Co}_{0.15}\text{Mn}_{0.15}\text{O}_2$ composite electrodes employing $\text{Li}_6\text{PS}_5\text{Cl}$. The fundamental performance of the all-solid-state battery is scrutinized by analyzing simulated physical and electrochemical behaviors in terms of mass transport and interfacial electrochemical reaction kinetics. The digital twin model herein reveals valuable but experimentally inaccessible time- and space-resolved information including dead particles, specific contact area, and charge distribution in the 3D domain. Thus, this new computational model is bound to rapidly improve the all-solid-state battery technology by saving the research resources and providing valuable insights.

David Gelernter's book "Mirror Worlds," published in 1991.^[1] In the early 2000s, this technique was realized by Michael Grieves in manufacturing processes and broadly employed in a variety of industrial and scientific fields.^[2] In particular, digital twin modeling that is applied to mechanical, thermal, and fluid dynamics simulations has been broadly verified and effectively utilized in numerous applications such as car crash testing, heat exchangers, and designing of airplane wings.^[3] With the unceasing progress in computer hardware and software technologies, the digital modeling and rapid simulation of much more complex objects with multi-scale structures has commenced.

Complex electrochemical behaviors in lithium-ion battery system has been an intriguing issue in this field, and are composed of heterogeneous reactions and various charge fluxes; the former only occurs at interfaces between the active material and electrolyte, whereas the latter, which involves the movement of electrons in the conductor and that of ions in the electrolyte, has to be unlimited to deliver a significant amount of charge to the interfaces.

Computational model that effectively emulates the above-mentioned complex physical phenomenon has already been achieved by the Newman group and broadly utilized thus far.^[4] When applying the approach of setting up additional pseudo dimensions for efficient particle simulation in complicated composite electrode structures, the approach must be very creative and practical for application to lithium-ion batteries. However, even if 3D modeling is conducted, the pseudo dimension method suffers from shortcomings, one of which is its inability to simulate and investigate local area problems. Thus, pseudo- x -dimensional models ($x = 2, 3, \text{ and } 4$) cannot be a complete digital twin model.^[5] This issue gets much more significant in other battery systems ongoing research and development to find problems in electrode/cell designs and gain insightful solutions for achieving beyond cell performance of lithium-ion batteries.

An all-solid-state battery with a solid sulfide electrolyte is one of the most promising post-lithium-ion batteries having a potential of high energy density and excellent safety.^[6] Samsung researchers reported a 0.6 A h class prototype pouch cell with a solid argyrodite sulfide electrolyte, which had an energy


1. Introduction

A digital twin is a virtual replica of an object or system in which the real shape and physical phenomena has been transferred into the digital space. The concept of a digital twin appeared in

J. Park, D. Jin, D. Kim, Prof. Y. M. Lee
Department of Energy Science and Engineering
Daegu Gyeongbuk Institute of Science and Technology (DGIST)
Daegu 42988, Republic of Korea
E-mail: yongmin.lee@dgist.ac.kr

K. T. Kim, Dr. D. Y. Oh, Prof. Y. S. Jung
Department of Chemical and Biomolecular Engineering
Yonsei University
Seoul 03722, Republic of Korea

K. T. Kim, Dr. D. Y. Oh, Prof. Y. S. Jung
Department of Energy Engineering
Hanyang University
Seoul 04763, Republic of Korea
E-mail: yoonsjung@hanyang.ac.kr

 The ORCID identification number(s) for the author(s) of this article can be found under <https://doi.org/10.1002/aenm.202001563>.

DOI: 10.1002/aenm.202001563

density greater than 900 W h L^{-1} and a long life of more than 1000 cycles at 0.5 C-rate and $60 \text{ }^\circ\text{C}$.^[7] Digitalization of the twin all-solid-state battery is thus urgently required to improve and optimize cell performance, and ultimately bring forward a product launch.

To date, there have been only a few reports that adopted the digital twin technique for all-solid-state batteries. Bielefeld et al. investigated the optimum ratio of active material and solid electrolyte by checking the utilization level of the connected particle clusters on the 3D electrode structure, including spherical active materials and sulfide-based solid electrolytes.^[8] Further, they studied the specific contact area and effective conduction with varying the amounts of binder.^[9] Shi et al. also predicted the loss in capacity by back-calculating the utilization of the cathode as a function of the material component ratio and the particle size.^[10] Although the critical parameters for estimating cell performance were obtained, the elaborate shape of the objects in the real electrode was not reflected and the electrochemical properties were not simulated. Ito et al. formed a 3D electrode structure with a realistic interface between the electrode materials on the basis of the phase-field method, and also numerically simulated the voltage and discharge capacity values.^[11] Park et al. tried to digitally copy the real all-solid-state electrode structure using analysis data from scanning electron microscopy (SEM) images, and predicted the electrochemical variables such as voltage, state of charge (SOC), and overpotential as well as the effective conductivities and contact area properties.^[12] Although fabrication of a digital twin all-solid-state electrode was achieved along with calculation of the electrochemical phenomena in the battery system, the theoretical electrochemical simulation was not conducted on a 3D digital twin structure. Finsterbusch et al. were successful in simulating the 3D electrochemical behavior of a solid oxide electrolyte-based electrode structure fabricated by 3D reconstruction of SEM tomography images.^[13] Neumann et al. also reported simulation results of a solid sulfide electrolyte-based electrode structure fabricated by 3D reconstruction of X-ray images.^[14] Although these studies came close to achieving the ultimate digital twin model, two remaining issues were yet to be improved; the challenges associated with fabricating a highly reliable digital twin structure and achieving a low deviation between simulation results and experimental data.

In this work, we first propose a new fabrication process for actual all-solid-state electrodes comprising of secondary particles of active materials ($\text{LiNi}_{0.70}\text{Co}_{0.15}\text{Mn}_{0.15}\text{O}_2$ [NCM]), solid sulfide electrolytes ($\text{Li}_6\text{PS}_5\text{Cl}$ [LPSCl]), and binders (nitrile butadiene rubber [NBR]). Second, we utilize digital twin electrodes, and introduce a methodology that analyzes the key properties directly related to cell performance in which specific physical values are used to verify the structures. Finally, the digital twin-driven all-solid-state battery based on a solid sulfide electrolyte is set up and used to predict electrochemical behaviors. The reliability of this model is also confirmed by comparing the simulated results with those of the experimental data.

2. Results and Discussion

Contrary to conventional 3D reconstruction techniques that are based on experimental tomographic images, our digital

twin electrode can be easily and quickly generated using only a few design parameters. The process for building a digital twin all-solid-state electrode with a secondary particle-type electrode active material, spherical solid sulfide electrolyte, and polymeric binder is as follows: first, temporary globular active material objects are drawn in a 3D domain by reflecting their particle size analysis (PSA) data. Second, polyhedral primary active material particles, that are size-confirmed from SEM image analysis, are scattered over the existing objects while removing the existing objects resulting in the real secondary particle active material. Third, because the solid sulfide electrolyte is deformable during the pressing process, they are located at the interspace of the active materials with reflecting their sizes from the PSA result. Thus, sufficient percolation pathways for lithium ions are generated whilst creating minimal porosity; this is key to limiting the number of inactive voids. Finally, the polymeric binder is added between all electrode and electrolyte particles.

The resulting digitally twinned all-solid-state electrodes consisting of NCM, LPSCl, and NBR are shown in **Figure 1a**. By applying the experimental particle size distributions and shapes of both the electrode active material and electrolyte particles (obtained from the PSA and SEM images, Figures S1 and S2, Supporting Information), digital twin electrodes with four different compositions (NCM:LPSCl = 60:38, 70:28, 80:18, and 90:8 wt%) were successfully created. As **Figure 1a** was generated based on random seed 1, we explored whether other random seeds formed similar digital twin structures under the same electrode design conditions (**Figure S3**, Supporting Information). A random seed is defined as an arbitrary number that assigns an initial location of the first object drawn. When comparing **Figure 1a** and **Figure S3**, Supporting Information, the digital twin electrodes with different random seeds have similar microstructural features if the electrode composition is the same. This repetitive process is required not only to estimate allowable errors originating from modeling and simulation, but also to overcome the limitations of local domain interpretation. As shown in **Figure 1a**, the four digital twin electrodes with different NCM contents of 60, 70, 80, and 90 wt% (hereafter, they are denoted as NCM 60 wt%, NCM 70 wt%, NCM 80 wt% and NCM 90 wt%, respectively) clearly reflect the designed or real morphologies (**Figure S4**, Supporting Information). In particular, the bumpy surface and inner pores of NCM secondary particles were delicately imitated (**Figure 1b,c**). Also, regardless of the much low content of NBR binder in comparison to NCM and LPSCl, **Figure S5**, Supporting Information, shows that the NBR binder is evenly distributed within the electrode over different random seeds (1–5). **Figure 1d** summarizes the average volume fraction of each component, with error ranges, depending on random seeds from 1 to 5. Each value is very close to the target values, depicted in the top region in **Figure 1a**, within a 2% error range. Thus, these results show that our digital twin formation process for all-solid-state electrode structures is highly reliable.

The digital twin all-solid-state electrodes were utilized to investigate the existence of dead particles, which are physically isolated from the surrounding identical materials. In the case of NCM, there were only one or two dead particles in the NCM 60 wt% electrode (**Figure S6**, Supporting Information).

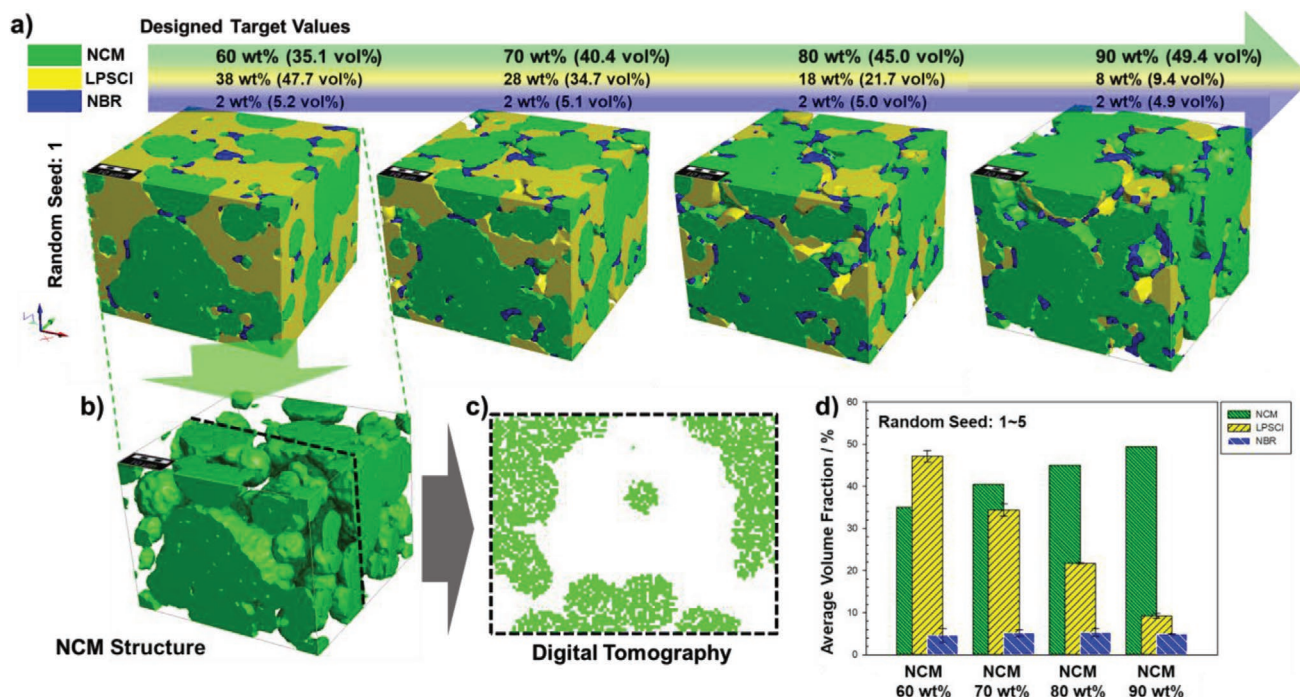


Figure 1. 3D digital twin all-solid-state NCM electrodes with varying the fraction of NCM. a) 3D digital twin all-solid-state electrodes of NCM 60, 70, 80, and 90 wt% on random seed 1. b) 3D structure and c) its corresponding 2D digital tomography image of NCM 60 wt%. d) Average volume fraction/error percentage of the electrode components on all random seeds as a function of NCM ratio.

As the maximum volume fraction of dead particles is less than 1%, its negative effects for the electrochemical performance should be marginal. The occurrence of dead particles disappears as NCM wt% increases owing to more stochastic connectivity. Similarly, more LPSCI dead particles are observed in proportion to NCM wt%, but their volume fraction does not exceed 0.5% up to the NCM 80 wt% electrode. However, when the composition of NCM is designed to be 90 wt%, the LPSCI dead particles increase significantly to approximately 6–20% (Figure S7, Supporting Information). These data indicate that the compositional design range from NCM 60 to 80 wt% (i.e., from LPSCI 38 to 18 wt%) is appropriate to achieve minimal dead particles within the all-solid-state electrode. In addition, when the specific contact area values between NCM and LPSCI are compared with or without dead particles (Figure S8, Supporting Information), the dead particle effect is insignificant in our electrode conditions. Furthermore, the decrease in specific contact area is quantified as a function of NCM wt%, which is closely related to electrochemical reaction sites. That is, as NCM wt% increases from 60 to 90 wt%, a higher surface overpotential occurs even if both electrons and ions are in sufficient supply.

Next, our digital twin all-solid-state NCM/LPSCI/NBR electrodes were utilized to investigate the effective electronic and ionic conduction behaviors via a stationary simulation on the basis of Ohm's law (Figure S9 and Table S1, Supporting Information). **Figure 2a,b** provides both simulated and experimental data as a function of NCM wt%, in which five simulated values are depicted as colored areas. Importantly, our digital twin electrodes could simulate both effective electronic and ionic conductivity values comparable to the real system. To our knowledge, this is

the first report of both simulated and experimental results based on genuine digital twin models. In addition, our digital twin models show logical trends that each effective conductivity range depends on the amount of corresponding conductive materials. In particular, the effective ionic conductivity values of the NCM 90 wt% electrodes could not be calculated due to disconnected percolation pathways between LPSCI particles. (Figure S10, Supporting Information). Another remarkable point in the simulated results is that the simulated conductivity range, described above as the colored areas, becomes larger as the corresponding conductive material decreases.

In addition, to determine electron and ion flow within the digital twin electrodes, a visual analysis was carried out (Figure 2c–f). As estimated from the effective electronic conductivity values, the NCM 80 wt% exhibits better electron density over the same domain than that of the NCM 60 wt% (Figure 2c,d). It should be noted that the electrodes did not contain conductive carbon materials to enhance the connectivity of the NCM particles. Considering ion conduction pathways, the NCM 60 wt% has a much higher ion density across more spatial regions. Thus, as the content of LPSCI decreases to 20 wt% (NCM 80 wt%), its ionic pathways become more localized than the electronic pathways in the NCM 60 wt%. These characteristics are also confirmed by comparing their refined volumes separated by a current density of over 20 mA cm⁻² (Figure S11a,b, Supporting Information). Moreover, when the ionic current density in the NCM 80 wt% is cut by over 80 mA cm⁻², the corresponding ionic pathway becomes more limited or only slightly connected (Figure S12, Supporting Information). Thus, as in this work, the blending ratios of NCM to LPSCI should be carefully designed to ensure favorable electronic and ionic

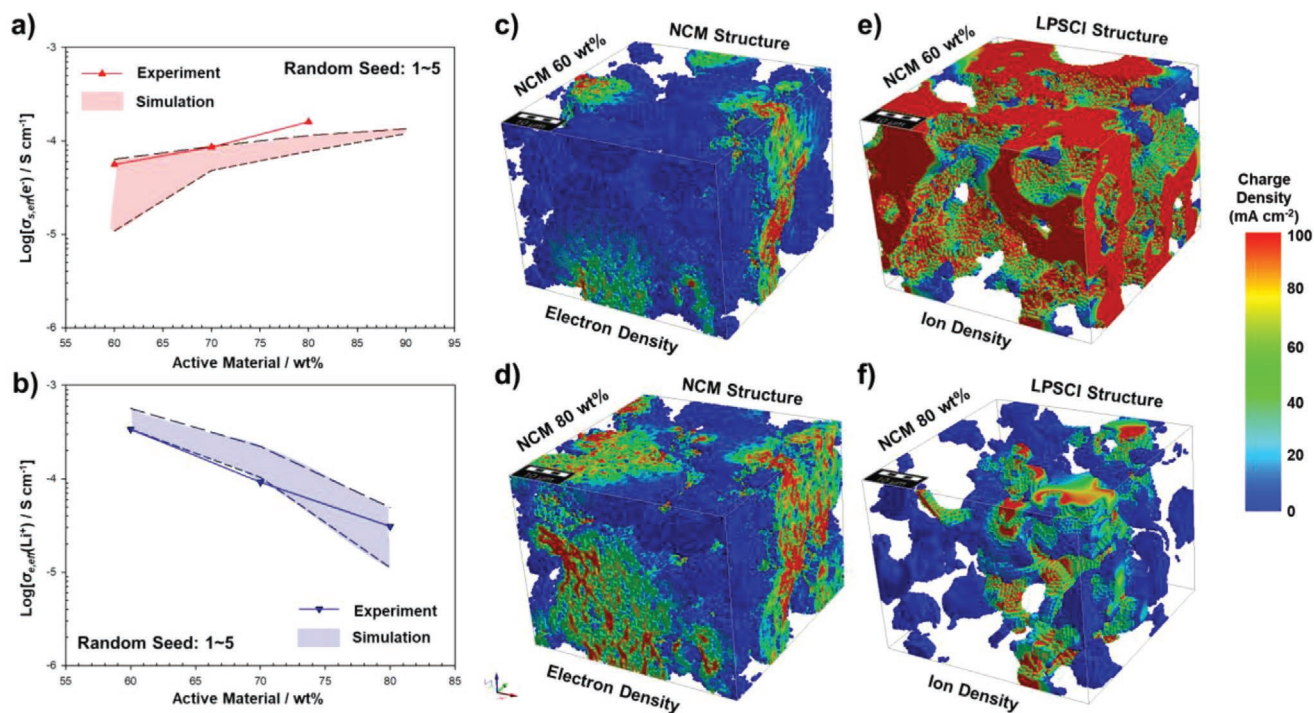


Figure 2. Comparative experimental data and simulation results of the effective a) electronic and b) ionic conductivities. Electron density in the NCM structure in c) NCM 60 and d) NCM 80 wt% electrodes. Li^+ ion density in the LPSCI structure in e) NCM 60 and f) NCM 80 wt% electrodes.

pathways of the active materials and solid electrolytes in the all-solid-state electrode. Therefore, depending on the intrinsic electronic or ionic conductivities of the electrode or electrolyte materials, the optimum composition ratios can be changed to achieve the required performance.

Simulation of the electrochemical performance is key to the successful design of digital twin all-solid-state NCM/LPSCI/NBR electrodes. To build a real digital twin battery model, a stacked electrochemical cell comprising lithium metal, an LPSCI electrolyte layer, an NCM/LPSCI/NBR electrode layer, and an aluminum layer in series was designed, as shown in Figure S13, Supporting Information. Next, equations governing the simulation of the dependent variables for lithium concentration, potential, overpotential, etc. were reflected in the digital twin cell (Figure S13 and Table S2, Supporting Information). The resulting rate capabilities for all the NCM 60, 70, or 80 wt% electrodes, at a C-rate of 0.1, 0.5, or 1C, are summarized in Figure 3. Slight variations at the same C-rate reflect those in each digital twin structure. To verify the reliability of our digital twin model, comparison of our simulation results with experimental data reported in previous studies, which had similar cell designs and operating conditions (Figure S12, Supporting Information), was performed.^[15] Notably, our simulated specific capacities were similar to the experimental data reported at a number of different C-rates. Moreover, the average capacity deviation of our model was very low, $\approx 12.5 \text{ mA h g}^{-1}$, whereas the latest study based on digital twin modeling and simulation reported much higher capacity deviation of around 80 mA h g^{-1} , especially at high current densities.^[14] In addition, the cell with NCM 70 wt% electrode/LPSCI layer/Li-In electrode was fabricated and evaluated at the same condition under which the digital twin-driven

model was operated. Amazingly, the simulated average capacity deviation at 1C was $\approx 11 \text{ mA h g}^{-1}$ while the values of the other works based on the electrode having the nanosized conductive materials were more than 12.5 mA h g^{-1} at 1C (Figure S14, Supporting Information). These improvements are ascribed to the higher accuracy of our digital twin electrodes with respect to their microstructures and the pre-checked parameters such as the effective electronic/ionic conductivities. Furthermore, considering the gravimetric specific capacities based on the mass of the NCM active material, it is evident that the specific capacity decreases with an increasing amount of NCM (Figure 3a–c). In particular, even at the lowest C-rate of 0.1C, considerable specific capacity reduction is observed as the NCM content increases from 60 to 80 wt% NCM, as high as 20 mA h g^{-1} , equivalent to 15%. This result is supported by a decrease in the specific contact area between NCM and LPSCI (Figure S8, Supporting Information). Also, the much larger decrease in the capacity ratio of NCM 80 wt% at higher C-rates supports the combined negative effects of both lower specific contact area and effective ionic conductivity of the electrode. From a practical point of view, checking the areal capacity based on the absolute mass of electrode materials is imperative (Figure 3d–f). Interestingly, both NCM 70 and 80 wt% electrodes exhibit slightly higher areal capacities than a NCM 60 wt% electrode at 0.1C. However, with slight increases in the C-rate up to 0.5C, the capacity falls in comparison to the NCM 60 wt%, which implies that an electrode design with a higher NCM content is not effective under high C-rate conditions. Based on the comprehensive interpretation and comparisons of the simulation results and experimental data thus far, it is clear that our digital twin-driven all-solid-state battery demonstrates the required performance.

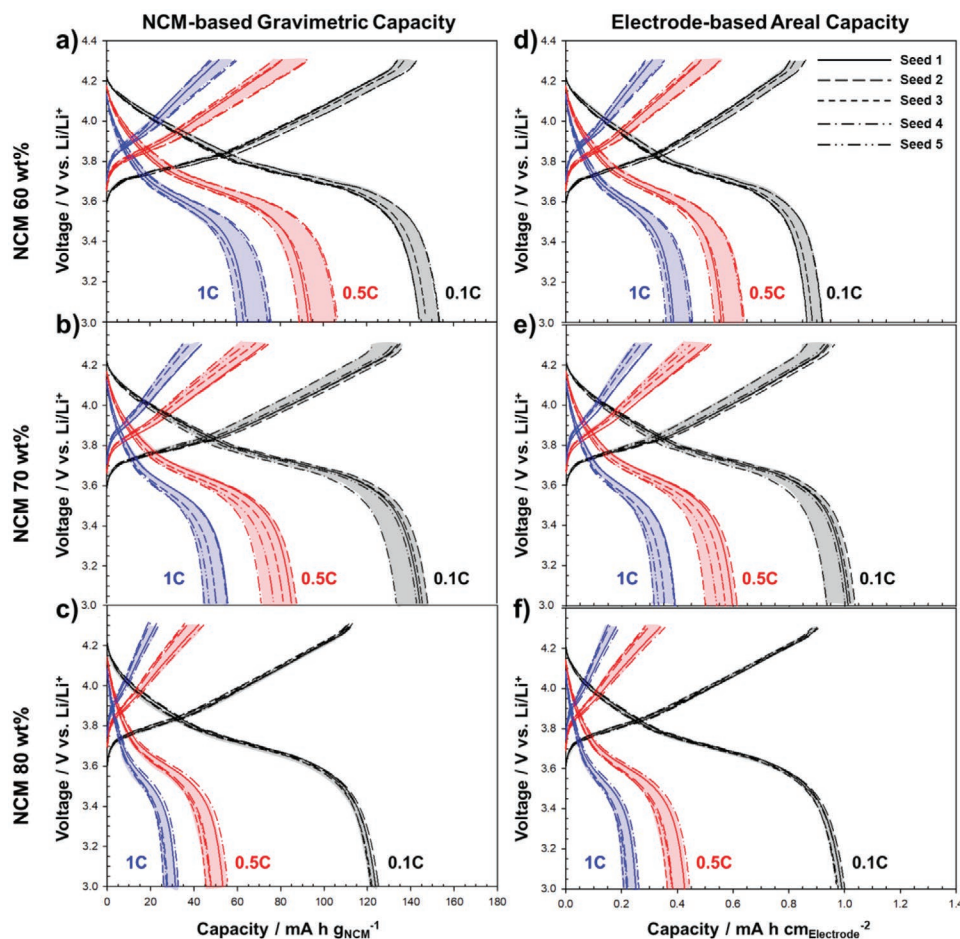


Figure 3. Voltage profiles with NCM-based gravimetric capacities for NCM a) 60, b) 70, and c) 80 wt%, and with electrode-based areal capacities for NCM d) 60, e) 70, and f) 80 wt% at various C-rates (0.1, 0.5, and 1C).

The most powerful aspect of the digital twin-driven model is the time- or space-resolved visualization. In this regard, the inferior performance of the NCM 80 wt% electrode, compared to that of the NCM 70 wt% electrode, can be digitally analyzed as if an operando experiment is conducted. **Figure 4** displays the distribution of SOC in the digital twin active materials of NCM 80 wt% at different current densities; this data indicates that the SOC value of cell is inversely proportional to the lithium concentration in the active material. **Figure 4a–c** shows the results obtained at the last moment after cell discharge (or lithiation process). The low current density relatively guaranteed a well-distributed and intercalated lithiation state, compared to that of middle or high current densities. The NCM 70 wt% electrode had more uniform lithium distribution and lithiation level in the active material particles than those of the NCM 80 wt% electrode (**Figure S15**, Supporting Information). Moreover, in-depth analysis of partial volumes with lithiation over 80% demonstrates that the NCM particles closer to the LPSCl electrolyte layer are more intercalated (**Figure S16**, Supporting Information). This result supports the interpretation that there is sufficient effective electronic conductivity in this electrode design. Even at the same voltage (about 3.5 V in this study), there is excellent lithiation distribution and density of active material

particles at lower current densities (**Figure 4d–f**). These analysis data are surely showing that NCM active materials in all-solid-state electrode cannot be perfectly lithiated or delithiated, and the concentration overpotential in active materials increases because the solid electrolyte particles are not infiltrated to the interstice of secondary particles. This issue should be solved on various approaches such as the use of nanolevel solid electrolyte for filling in pore and the lattice control of active materials for higher lithium-ion diffusivity.

In contrast to that observed for the active material, the concentration gradient of lithium-ions in the solid sulfide electrolyte is not present because the inorganic solid electrolyte is a single-ion conductor with a transference number of approximately 0.99–1. Hence, the analysis of the movement of lithium-ions in the solid electrolyte is performed using the flux density value. **Figure 5** shows the analysis data for ion flux at the solid electrolyte in NCM 70 and 80 wt% electrodes under C-rate conditions of 0.1 and 1C. As a neutral charge balance must be maintained, the amount of ion flux depends on the current density value. Thus, there is a natural increase in the ion flux value with an increasing current density; such ion flux behaviors at high current density are replicated for both NCM 70 (**Figure 5a,b**) and 80 wt% electrodes (**Figure 5c,d**). It is remarkable to note that the ion flux simulated

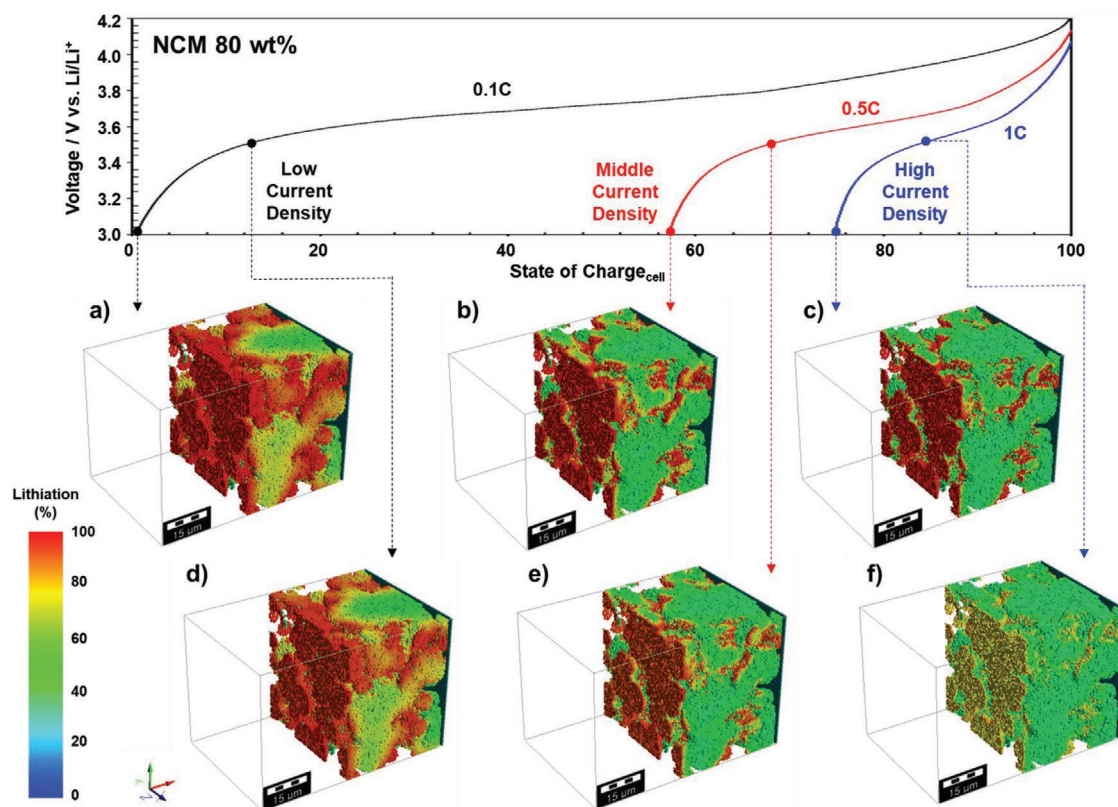


Figure 4. Lithiation at the last moment of discharge for a cell in the charged state at a) 0.1C, b) 0.5C, and c) 1C at 3.0 V and at d) 0.1C, e) 0.5C, and f) 1C at 3.5 V.

from the 80 wt% electrode is higher and less uniform than that from the 70 wt% electrode. This is a result of the higher amount of active material in the 80 wt% electrode leading to higher ion flux. In addition, the lower amount of solid electrolyte in the 80 wt% electrode results in narrower and more complicated ion pathways. The problem associated with the NCM 80 wt% electrode thus results in higher ohmic resistance in the solid electrolyte network as a result of mass transport limitations. That is why the new solid electrolyte materials, which have higher intrinsic ionic conductivity and better deformation property for minimizing the tortuosity, have been extensively investigated.

In **Figure 6**, we show the effect of electrochemical reaction site in relation to the surface overpotential values, obtained at the last moment after discharging at 0.1C and 1C, for the active materials in the NCM 70 and 80 wt% electrodes. In the case of the NCM 70 wt% electrode, the overpotential values formed at low C-rates are much lower than those at high C-rates (Figure 6a,b). However, the overpotential values at low C-rates in the NCM 80 wt% electrode are already relatively high, compared to those at high C-rates (Figure 6c,d). In Figure S17, Supporting Information, we also predicted similar overpotential behavior as positive numbers during charging. These significant surface overpotential values can be correlated to the relatively low specific contact area in comparison to the amount that is required for the electrochemical reaction to proceed. Thus, from the perspective of mass transport and electrochemical reaction rate kinetics, these data visually demonstrate why the rate capability of the 80 wt% electrode was poor in comparison to the other electrodes (Figure 3). This issue

has been solved by coating or doping specific materials (LiNbO₃, lithium halide, etc.) on electrode materials for faster electrochemical reaction rate and less side reactions on the interface of the active materials and solid electrolytes.

As we have previously discussed, the digital twin all-solid-state electrode or battery provide powerful solution to be able to analyze physical properties, such as isolated particles, contact area between constituents, and effective conductivity, as well as the prediction of operando electrochemical properties at any time and location. Of course, the impact of this technology is actually dependent on how elaborate the resulting fabricated digital twin structure is. Once perfect digital twin electrodes are successfully created, a significant amount of highly reliable analysis, which is considered experimentally challenging, can be achieved. At the same time, this data can be utilized to explore or optimize the electrode and cell designs with a minimal requirement for experimental procedures (**Figure 7**). This report of our digital twin-driven model and simulation is the first step in gaining the optimum design parameters for high performance all-solid-state batteries, and our model is a strong contender to be the unrivaled numerical model that provides the fundamental insight.

3. Conclusion

We successfully designed a new formation process for a digital twin all-solid-state electrode with a solid sulfide electrolyte

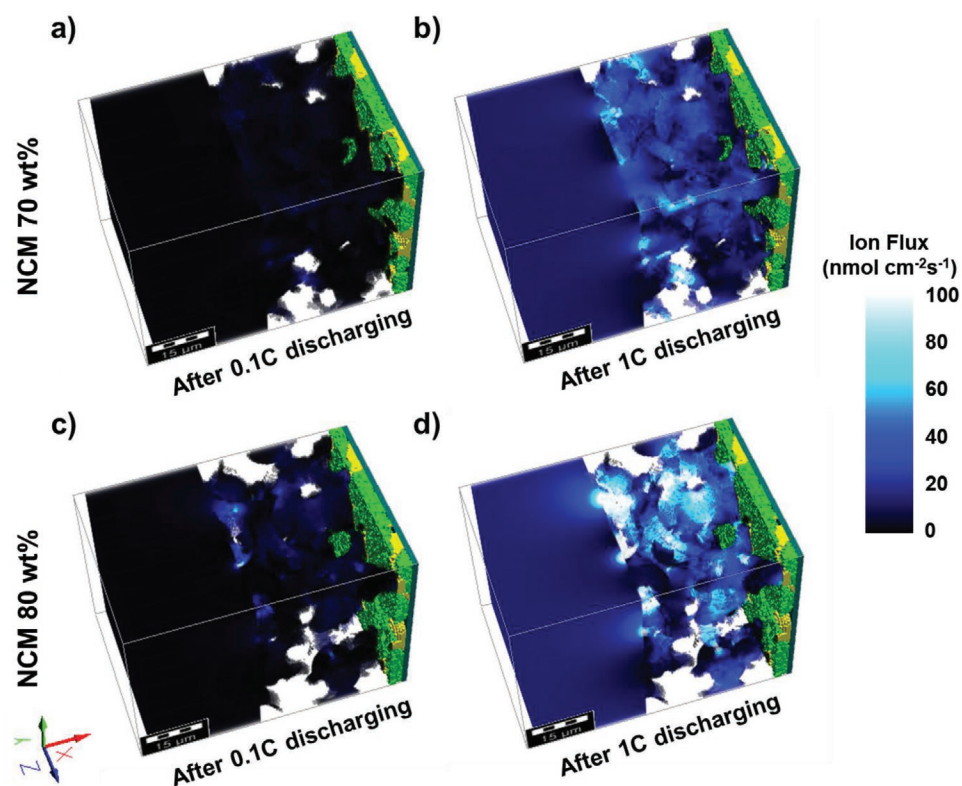


Figure 5. Ion (Li^+) flux of the NCM 70 wt% electrode at the last moment after discharging at a) 0.1C and b) 1C and of the NCM 80 wt% electrode at the last moment after discharging at c) 0.1C and d) 1C.

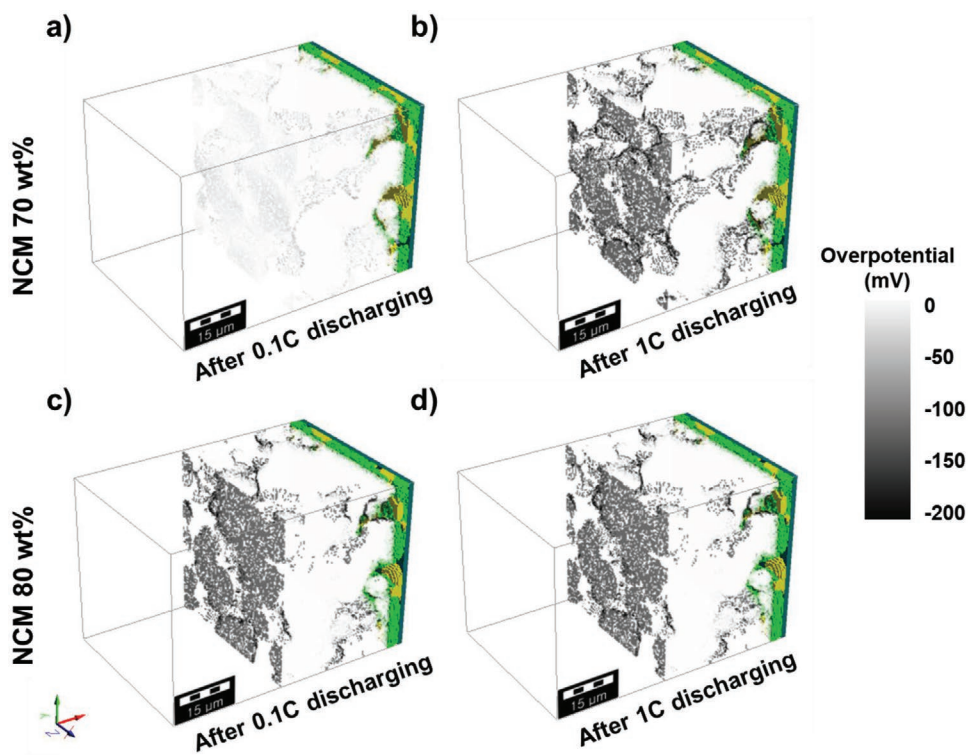


Figure 6. Surface overpotential of the NCM 70 wt% electrode at the last moment after discharging at a) 0.1C and b) 1C and of the NCM 80 wt% electrode at the last moment after discharging at c) 0.1C and d) 1C.

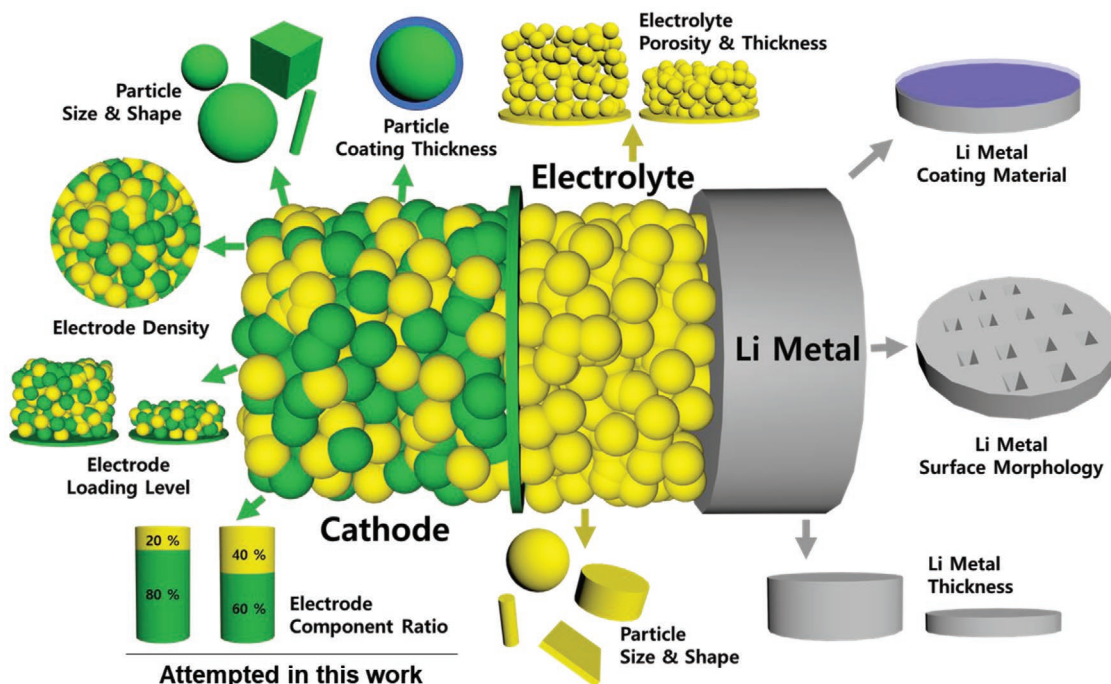


Figure 7. Design parameters for an all-solid-state battery with a solid sulfide electrolyte and lithium metal electrode.

without numerous tomography images and verified that our virtual electrodes matched real electrodes by comparing both experimental and calculated effective conductivity values. In particular, our digital twin electrodes provided important physical and electrochemical parameters such as dead particles, specific contact area, effective electronic/ionic conductivities, and charge distribution in the 3D domain. In addition, operando analysis and the electrochemical performance at different C-rates was simulated in the digital twin all-solid-state electrode, providing valuable insight into the electrochemical cell. A high correlation between the simulated and experimental data demonstrates the high reliability of our digital twin-driven model. Furthermore, the simulated lithiation level in the active materials, ion flux in the solid electrolyte, and surface overpotential of the electrochemical reaction sites were utilized to understand the underlying electrochemical processes. Thus, our digital twin-driven all-solid-state battery provides significant results for the cell's design parameter optimization that needs more effort and resources by experiments, such as assembling and testing cells.

4. Experimental Section

Building the Digital Twin All-Solid-State Electrodes: The virtual all-solid-state electrodes, which consist of LiNbO_3 -coated $\text{LiNi}_{0.7}\text{Co}_{0.15}\text{Mn}_{0.15}\text{O}_2$ (NCM, 4.44 g cm^{-3} , particle porosity: 32.7%), $\text{Li}_6\text{PS}_5\text{Cl}$ (LPSCI, 2.07 g cm^{-3}), and nitrile butadiene rubber (NBR, 1.00 g cm^{-3})^[15c,16] were digitally drawn using different ratios of NCM and LPSCI (NCM:LPSCI:NBR = 60:38:2, 70:28:2, 80:18:2, and 90:8:2, wt%) under the electrode design conditions of 10 mg cm^{-2} and $\approx 39 \mu\text{m}$ (electrode density: $2.5\text{--}2.6 \text{ g cm}^{-3}$). For this work, a GrainGeo module in GeoDict 2020 was used and the formation process was as follows: uniform spherical NCM active material objects were made in the 3D domain of $50 \mu\text{m} \times 50 \mu\text{m} \times \approx 39 \mu\text{m}$ size with the

cubic voxels of $0.5 \mu\text{m}$ edge under a random seed number (1–5) using the particle size analysis data (Figure S1, Supporting Information), then the polyhedral primary active materials, based on SEM image analysis data (Figure S2, Supporting Information), were positioned on the existing objects at the same time as removing the existing objects. Next, the spherical NCM objects were overlapped with the structure of the polyhedral primary active materials, and the solid electrolyte particles, based on particle size analysis data (Figure S1, Supporting Information), were located at the interspace of the overlapped active materials whilst maintaining the initial random seed number; then, a polymeric binder was added between all particles. Finally, the NCM primary active materials, the LPSCI solid electrolyte particles, and the NBR binder structures were combined to form a composite electrode structure. The above-mentioned process for the formation of electrode materials' objects was accompanied with the periodic function that allows the generation of a whole object by forming the cut particle volume on the opposite side without substituting for small particles.

Preparation of Materials: For the LPSCI, a stoichiometric mixture of Li_2S (99.9%, Alfa Aesar), P_2S_5 (99%, Sigma Aldrich), and LiCl (99.99%, Sigma Aldrich), and was mechanically ball-milled at 600 rpm for 10 h in a ZrO_2 vial with ZrO_2 balls using Pulverisette 7PL (Fritsch GmbH). The resulting powders were annealed at $550 \text{ }^\circ\text{C}$ for 5 h. Wet-chemical coatings of LiNbO_3 on NCM powders (0.5 wt%) were carried out using lithium ethoxide (95%, Sigma Aldrich), niobium ethoxide (99.95%, Sigma Aldrich), and anhydrous ethanol (99.9%, Sigma Aldrich). NBR were purchased from Sigma Aldrich. All processes were conducted in the Ar-filled glove box.

Fabrication of Electrodes: The NCM electrodes were fabricated by slurry method using dibromomethane as a processing solvent, as described in a previous report by the authors.^[15c] The wet slurries consisting of targeting weight ratios of NCM, LPSCI, and NBR were coated on Ni foil to measure electrical conductivities of electrodes, or carbon-coated foil for Al foil to measure electrochemical performance by doctor-blade method and the subsequent drying at $60 \text{ }^\circ\text{C}$ under vacuum. The weight ratios of NCM, LPSCI, and NBR were 60:38:2, 70:28:2, and 80:18:2.

Material Characterization: For the cross-sectional field emission scanning electron microscopy (FESEM) measurements, electrode

samples were polished with an Ar ion beam initially at 6 kV for 6 h and then at 4 kV for 3 h (JEOL, IB19510CP). FESEM images were obtained using AURIGA (Zeiss). To avoid any air exposure to the polished samples, an airtight transfer box, DME 2830 (SEMILAB), was used.

Conductivity Measurements and Electrochemical Characterization: The effective electronic conductivities of the NCM electrodes were obtained by four-probe Van der Pauw method under an applied pressure of 100 MPa.^[17] The effective ionic conductivities of the NCM electrodes were measured by AC impedance method using e⁻-blocking Li-In/LPSCI/ electrode/LPSCI/Li-In symmetric cells. The EIS data were collected with an amplitude of 14 mV and a frequency range from 10 mHz to 7 MHz using an Iviumstat (IVIUM Technologies Corp.). All the measurements were conducted at 30 °C. For the measurements of electrochemical performances, NCM/Li-In half cells were fabricated and evaluated. The Li-In counter electrodes (Li_{0.5}In:LPSCI = 80:20 wt%) were prepared by ball-milling In (Aldrich, 99%), Li (FMC Lithium Corp.), and LPSCI powders. 150 mg of LPSCI was pelletized under 100 MPa to form the solid electrolyte layer. Then, the as-prepared sheet-type electrodes and Li-In electrode were placed on each side of the solid electrolyte layer. Finally, the all-solid-state NCM/Li-In half cells were fabricated by pelletizing at 370 MPa.

Calculation of Physical Properties from Digital Twin Structures: Using the digital twin all-solid-state electrodes, isolated particles of NCM and LPSCI were analyzed under activated flow boundary conditions using the function of Open and Closed Porosity in a PoroDict module in GeoDict 2020. The specific contact area values between the NCM and LPSCI particles were also calculated using statistical analysis based on Minkowski measures (volume, surface, integral of mean, integral of total curvature) through the PoroDict module. The effective conductivities ($\sigma_{s,eff}/\sigma_{e,eff}$) were calculated by considering the volume fraction ($\varepsilon_s/\varepsilon_e$) and tortuosity (τ_s/τ_e) of conductive materials to intrinsic electronic/ionic conductivity value (σ_s/σ_e) at 30 °C, and the magnitude of current density (j) was simulated on the basis of the governing equation of Ohm's law which relates the electric/electrolyte potential (ϕ_s/ϕ_e) (Equation S1 and S2 in Figure S9, Supporting Information). The boundary conditions were set up as $\Delta V = 1$ V under the Dirichlet condition that assigns the constant potential value on the plane. The explicit jump (EJ) solver that has high advantages of solving the porous structure was used for this simulation. All process implemented by using a ConductoDict module in GeoDict 2020 (Figure S9 and Table S1, Supporting Information).^[11,15d,16]

Predicting Electrochemical Performance and Behavior using the Digital Twin-Driven Model: The function of Design Battery in a BatteryDict of GeoDict 2020 was used for the set-up of a digital twin stacked cell with the composition lithium metal (3 μ m)/LPSCI layer (30 μ m)/all-solid-state electrode/aluminum (1.5 μ m). The governing equations (Butler–Volmer, mass balance, and charge balance equations) and parameters were assigned on the corresponding materials (Figure S13 and Table S2, Supporting Information).^[12,16d,18,19] The Butler–Volmer equation (Equation S3 in Figure S13, Supporting Information) simulates the current density (j_{se}) on interfaces between active materials and electrolyte by reflecting the dependent variables of concentration (c_s/c_e) and potential (ϕ_s/ϕ_e), which are able to interpret the kinetics of electrode reaction based on mass transfer. The simulated current density values on the digital twin electrode are formulated with normal factor (\bar{n}) as an interface flux given by Equations S4 and S5 in Figure S13, Supporting Information. This current flux value is used for the boundary condition or the independent variable. The mass balance equations with intrinsic diffusion coefficient (D_s/D_e) are applied to each solid and electrolyte phase (Equations S6 and S7 in Figure S13, Supporting Information), and they can simulate the lithium concentrations (c_s/c_e) with the boundary conditions of current fluxes in a view of diffusion and migration. Herein, the lithium transference number (t_+) was set as 0.99 because the LPSCI solid electrolyte is the single-ion conductor. The charge balance equations (Equations S8 and S9 in Figure S13, Supporting Information) simulate the potentials of solid and electrolyte phases by considering intrinsic conductivity values (σ_s/σ_e) and current flux values. The differential relationship between concentration and potential in electrolyte is also reflected to calibrate the detail potential variation (First term on the right

side in Equation S8 in Figure S13, Supporting Information). The inactive volumes of the pore and binder materials are described by no-flux conditions to neighboring phases. Moreover, the outermost boundaries of cell have no-flux conditions. All process proceeded by the Charge Battery (BESTmicro solver, Battery and Electrochemical Simulation Tool micro, Fraunhofer ITWM, Germany). The digital twin all-solid-state batteries with different composite electrodes were each driven at 30 °C as a function of C-rate (0.1, 0.5, and 1C).

Supporting Information

Supporting Information is available from the Wiley Online Library or from the author.

Acknowledgements

J.P. and K.T.K. contributed equally to this work. This research was supported by the Technology Development Program to Solve Climate Changes of the National Research Foundation (NRF) funded by the Ministry of Science & ICT (NRF-2017M1A2A2044493 and 2017M1A2A2044501) and Creative Materials Discovery Program of the National Research Foundation (NRF) funded by the Ministry of Science & ICT (2020M3D1A1068764). The authors are also very thankful for the support from the DGIST Supercomputing and Bigdata Center.

Conflict of Interest

The authors declare no conflict of interest.

Keywords

all-solid-state batteries, all-solid-state electrodes, digital twins, electrochemical behaviors, sulfide solid electrolytes

Received: May 8, 2020

Revised: June 19, 2020

Published online:

- [1] D. Gelernter, *Mirror Worlds: Or: The Day Software Puts the Universe in a Shoebox... How It Will Happen and What It Will Mean*, Oxford University Press, Oxford **1993**.
- [2] S. Flumerfelt, K. G. Schwartz, D. Mavris, S. Briceno, *Complex Systems Engineering: Theory and Practice*, American Institute of Aeronautics and Astronautics, Reston, VA **2019**.
- [3] a) M. Borovinšek, M. Vesenjaj, M. Ulbin, Z. Ren, *Eng. Fail. Anal.* **2007**, *14*, 1711; b) A. Hickey, S. Xiao, *IJMSME* **2017**, *3*, 1; c) W. Q. Tao, Y. P. Cheng, T. S. Lee, *Heat Mass Transf.* **2007**, *44*, 125; d) M. Khoshvaght-Aliabadi, S. Zangouei, F. Hormozi, *Int. J. Therm. Sci.* **2015**, *88*, 180; e) D. You, P. Moin, **2006**; f) X. Chen, G.-C. Zha, M.-T. Yang, *Comput. Fluids*. **2007**, *36*, 856.
- [4] a) M. Doyle, T. F. Fuller, J. Newman, *J. Electrochem. Soc.* **1993**, *140*, 1526; b) J. Newman, K. E. Thomas, H. Hafezi, D. R. Wheeler, *J. Power Sources* **2003**, *119–121*, 838; c) Y. Xie, J. Li, C. Yuan, *Electrochim. Acta* **2014**, *127*, 266; d) W. Lai, F. Ciucci, *Electrochim. Acta* **2011**, *56*, 4369; e) W. A. Appiah, J. Park, S. Song, S. Byun, M.-H. Ryou, Y. M. Lee, *J. Power Sources* **2016**, *319*, 147; f) J. Park, W. A. Appiah, S. Byun, D. Jin, M.-H. Ryou, Y. M. Lee, *J. Power Sources* **2017**, *365*, 257.

- [5] a) K. Darcovich, D. D. MacNeil, S. Recoskie, B. Kenney, *Appl. Therm. Eng.* **2018**, *133*, 566; b) J. Park, J. Jeong, Y. Lee, M. Oh, M.-H. Ryou, Y. M. Lee, *Adv. Mater. Interfaces* **2016**, *3*, 1600140; c) J. Park, D. Kim, D. Jin, C. Phatak, K. Y. Cho, Y.-G. Lee, S. Hong, M.-H. Ryou, Y. M. Lee, *J. Power Sources* **2018**, *408*, 136; d) H. Li, C. Liu, A. Saini, Y. Wang, H. Jiang, T. Yang, L. Chen, C. Pan, H. Shen, *J. Power Sources* **2019**, *438*, 226974; e) J. Song, J. Park, W. A. Appiah, S.-S. Kim, H. Munakata, K. Kanamura, M.-H. Ryou, Y. M. Lee, *Nano Energy* **2019**, *62*, 810.
- [6] a) Y. Kato, S. Hori, T. Saito, K. Suzuki, M. Hirayama, A. Mitsui, M. Yonemura, H. Iba, R. Kanno, *Nat. Energy* **2016**, *1*, 16030; b) K. H. Park, Q. Bai, D. H. Kim, D. Y. Oh, Y. Zhu, Y. Mo, Y. S. Jung, *Adv. Energy Mater.* **2018**, *8*, 1800035; c) Z. Zhang, Y. Shao, B. Lotsch, Y.-S. Hu, H. Li, J. Janek, L. F. Nazar, C. Nan, J. Maier, M. Armand, L. Chen, *Energy Environ. Sci.* **2018**, *11*, 1945; d) R. Chen, Q. Li, X. Yu, L. Chen, H. Li, *Chem. Rev.* **2020**, *120*, 6820; e) N. Kamaya, K. Homma, Y. Yamakawa, M. Hirayama, R. Kanno, M. Yonemura, T. Kamiyama, Y. Kato, S. Hama, K. Kawamoto, A. Mitsui, *Nat. Mater.* **2011**, *10*, 682; f) X. Han, Y. Gong, K. K. Fu, X. He, G. T. Hitz, J. Dai, A. Pearse, B. Liu, H. Wang, G. Rubloff, Y. Mo, V. Thangadurai, E. D. Wachsman, L. Hu, *Nat. Mater.* **2017**, *16*, 572; g) Y. Chen, Z. Wang, X. Li, X. Yao, C. Wang, Y. Li, W. Xue, D. Yu, S. Y. Kim, F. Yang, A. Kushima, G. Zhang, H. Huang, N. Wu, Y.-W. Mai, J. B. Goodenough, J. Li, *Nature* **2020**, *578*, 251; h) A. Manthiram, X. Yu, S. Wang, *Nat. Rev. Mater.* **2017**, *2*, 16103; i) M. Li, C. Wang, Z. Chen, K. Xu, J. Lu, *Chem. Rev.* **2020**, *120*, 6783; j) Q. Zhao, S. Stalin, C.-Z. Zhao, L. A. Archer, *Nat. Rev. Mater.* **2020**, *5*, 229; k) C. S. Jjiang, N. Dunlap, Y. J. Li, H. Guthrey, P. Liu, S. H. Lee, M. M. Al-Jassim, *Adv. Energy Mater.* **2020**, *10*, 2000219.
- [7] Y.-G. Lee, S. Fujiki, C. Jung, N. Suzuki, N. Yashiro, R. Omoda, D.-S. Ko, T. Shiratsuchi, T. Sugimoto, S. Ryu, J. H. Ku, T. Watanabe, Y. Park, Y. Aihara, D. Im, I. T. Han, *Nat. Energy* **2020**, *5*, 299.
- [8] A. Bielefeld, D. A. Weber, J. Janek, *J. Phys. Chem. C* **2019**, *123*, 1626.
- [9] A. Bielefeld, D. A. Weber, J. Janek, *ACS Appl. Mater. Interfaces* **2020**, *12*, 12821.
- [10] T. Shi, Q. Tu, Y. Tian, Y. Xiao, L. J. Miara, O. Kononova, G. Ceder, *Adv. Energy Mater.* **2020**, *10*, 1902881.
- [11] Y. Ito, S. Yamakawa, A. Hayashi, M. Tatsumisago, *J. Mater. Chem. A* **2017**, *5*, 10658.
- [12] a) J. Park, D. Kim, W. A. Appiah, J. Song, K. T. Bae, K. T. Lee, J. Oh, J. Y. Kim, Y.-G. Lee, M.-H. Ryou, Y. M. Lee, *Energy Storage Mater.* **2019**, *19*, 124; b) J. Park, J. Y. Kim, D. O. Shin, J. Oh, J. Kim, M. J. Lee, Y.-G. Lee, M.-H. Ryou, Y. M. Lee, *Chem. Eng. J.* **2020**, *391*, 123528.
- [13] M. Finsterbusch, T. Danner, C. L. Tsai, S. Uhlenbruck, A. Latz, O. Guillon, *ACS Appl. Mater. Interfaces* **2018**, *10*, 22329.
- [14] A. Neumann, S. Randau, K. Becker-Steinberger, T. Danner, S. Hein, Z. Ning, J. Marrow, F. H. Richter, J. Janek, A. Latz, *ACS Appl. Mater. Interfaces* **2020**, *12*, 9277.
- [15] a) D. Y. Oh, D. H. Kim, S. H. Jung, J.-G. Han, N.-S. Choi, Y. S. Jung, *J. Mater. Chem. A* **2017**, *5*, 20771; b) Y. J. Nam, D. Y. Oh, S. H. Jung, Y. S. Jung, *J. Power Sources* **2018**, *375*, 93; c) D. Y. Oh, Y. J. Nam, K. H. Park, S. H. Jung, K. T. Kim, A. R. Ha, Y. S. Jung, *Adv. Energy Mater.* **2019**, *9*, 1802927; d) Y. J. Nam, K. H. Park, D. Y. Oh, W. H. An, Y. S. Jung, *J. Mater. Chem. A* **2018**, *6*, 14867.
- [16] a) A. Chakraborty, S. Kunnikuruvaan, M. Dixit, D. T. Major, *Isr. J. Chem.* **2020**, *60*, 1; b) H. Zhang, H. Zhao, M. A. Khan, W. Zou, J. Xu, L. Zhang, J. Zhang, *J. Mater. Chem. A* **2018**, *6*, 20564; c) X. Ge, Y. Zhang, F. Deng, U. R. Cho, *Polym. Compos.* **2017**, *38*, 2347; d) X. Li, L. Jin, D. Song, H. Zhang, X. Shi, Z. Wang, L. Zhang, L. Zhu, *J. Energy Chem.* **2020**, *40*, 39; e) L. Wang, B. Chen, J. Ma, G. Cui, L. Chen, *Chem. Soc. Rev.* **2018**, *47*, 6505.
- [17] a) L. J. Pauw, *Philips Tech. Rev.* **1958**, *20*, 220; b) Y. S. Jung, A. S. Cavanagh, A. C. Dillon, M. D. Groner, S. M. George, S.-H. Lee, *J. Electrochem. Soc.* **2010**, *157*, A75.
- [18] a) S. Wang, M. Yan, Y. Li, C. Vinado, J. Yang, *J. Power Sources* **2018**, *393*, 75; b) S.-K. Jung, H. Gwon, S.-S. Lee, H. Kim, J. C. Lee, J. G. Chung, S. Y. Park, Y. Aihara, D. Im, *J. Mater. Chem. A* **2019**, *7*, 22967; c) L. Froboese, J. F. v. d. Sichel, T. Loellhoeffel, L. Helmers, A. Kwade, *J. Electrochem. Soc.* **2019**, *166*, A318; d) L. E. Camacho-Forero, P. B. Balbuena, *Chem. Mater.* **2020**, *32*, 360; e) G. Hu, Y. Tao, Y. Lu, J. Fan, L. Li, J. Xia, Y. Huang, Z. Zhang, H. Su, Y. Cao, *ChemElectroChem* **2019**, *6*, 4773; f) A. Latz, J. Zausch, *J. Power Sources* **2011**, *196*, 3296.
- [19] a) A. Latz, J. Zausch, *Beilstein J. Nanotechnol.* **2015**, *6*, 987; b) S. Hein, A. Latz, *Electrochim. Acta* **2016**, *201*, 354; c) T. Danner, M. Singh, S. Hein, J. Kaiser, H. Hahn, A. Latz, *J. Power Sources* **2016**, *334*, 191; d) L. O. Valoen, J. N. Reimers, *J. Electrochem. Soc.* **2005**, *152*, A882.